energies

Article

Analytical Minimization of Interior Permanent Magnet Machine Torque Pulsations by Design of Sculpted Rotor

Steven Hayslett [1], Thang Pham [2] and Elias Strangas [2,*]

[1] Department of Mechanical Engineering, Michigan State University, East Lansing, MI 48824, USA; hayslet4@msu.edu
[2] Department of Electrical and Computer Engineering, Michigan State University, East Lansing, MI 48824, USA; phamtha1@msu.edu
* Correspondence: strangas@egr.msu.edu

Abstract: A new and efficient analytical optimization methodology for the design of rotor features is developed and used in interior permanent magnet motors (IPM). The analytical methodology is based on an extended winding function theory to include the IPM rotor's primary and secondary reluctance paths and the non-homogeneous airgap of the rotor sculpt features. The shape and placement of the rotor features, derived from the analytical-based optimization process, show the improvement in torque average and torque ripple of the IPM machine at a fraction of computational effort. The analytical optimization results are validated with finite element analysis via an exhaustive search.

Keywords: interior permanent magnet; rotor sculpting; torque ripple; MMF; permeance; winding function; optimization; analytical model; harmonics

check for updates

Citation: Hayslett, S.; Pham, T.; Strangas, E. Analytical Minimization of Interior Permanent Magnet Machine Torque Pulsations by Design of Sculpted Rotor. *Energies* **2022**, *15*, 4124. https://doi.org/10.3390/en15114124

Academic Editors: Ivan Yatchev and Hartmut Brauer

Received: 3 May 2022
Accepted: 1 June 2022
Published: 3 June 2022

1. Introduction

Increasing utilization of the interior permanent magnet (IPM) machine for propulsion applications is due to its good efficiency, torque, and power density. Examples include the development of battery electric vehicle traction motors [1,2], plug-in hybrid electric vehicles [3], and hybrid electric vehicles [4,5]. Ideally, the traction machine provides an average torque produced from a sinusoidal distribution of the airgap flux density. In reality, embedding the magnet within the salient structure of the rotor and distributing windings in discrete locations result in airgap flux density spatial harmonics. These harmonics result in increased torque ripple, radial forces, losses, and other unwanted phenomena.

Torque ripple is a persistent problem with IPM machines. Finite elements (FE) along with the design of experiments are commonly used to minimize torque harmonics; the integrated approach requires significant computational resources with little analytical insight. In [6,7], the choices of winding, rotor barrier placement, and their effects on magnetomotive force (MMF) are outlined via FE. However, the equivalent analytical models are not fully developed. Torque pulsations are minimized in [8] using only FE along with optimization to design rotor features. Pole shaping, both circumferential and axial, offers some ability to reduce torque ripple with minimal impact to average torque [9]. Genetic algorithms using a grid-on grid-off approach for rotor sculpting are shown to reduce torque harmonics with a slight increase to average torque [10], no analytical description is provided. A general expression of IPM torque harmonics is developed in [11]. Without a direct connection to the developed analytical equations, FE is used to drive individual torque harmonics to near zero.

Analytical modeling of the machine provides insight into the mechanisms of the machine and can be used to direct design. The IPM machine was modeled with magnetic equivalent circuits (MEC) in [12], showing good agreement in flux densities, losses, and torque properties but did not extend to design. Koo and Nam utilized MMF permeance methods in [13] for the IPM machine approximating the machine's salient feature permeance with a Taylor series to calculate torque harmonics and compared results between FE and analytical methods. A combination of surface and spoke type magnets were modeled in [14] showing better utilization of magnet mass for torque production establishing the principles of operation for a new rotor topology. Lee, Fan, and Wen accounted for the overall effects pole cap of the IPM machine salient structure in [15] for prediction of radial flux density but did not extend to torque harmonics or design. Analytical modeling of slots based upon magnetic dipole equivalent magnetic currents (EMC) was shown possible [16] and the equivalent magnetic dipole [17] used in conjunction with sub-domain modeling. The IPM sculpted rotor airgap flux density and torque are analytically modeled in [18] and focused on feature effects rather than optimal design. Analytical models have been used to provide trends and general observations and reduce computational effort but do have limits in predicting the physical effects of fringing and saturation. To date, there is limited work in determining IPM machine geometry, which minimizes torque pulsations, through the application of analytical models.

A two-part rotor was used in [19] to achieve peak reluctance and peak magnet torque simultaneously. The multi-barrier IPM rotor structure was modified with torque aligning surface magnets in [20]. A wound field synchronous structure was used with interior magnets to achieve optimal torque in [21]. Reluctance torque was preserved in the aligned axis IPM structure presented in [22]. The effectiveness of IPM rotor sculpting was presented in [23] shown to increase average torque. To date research has focused on the use of asymmetrical features, to increase average torque by aligning the magnet and reluctance torque. This has only considered the impacts on the fundamental airgap flux densities and has not considered the effects on the asymmetrical flux and torque harmonics and how to exploit them.

In this paper, an analytical approach to minimizing IPM machine torque ripple through the optimal design of asymmetrical sculpt features is presented. Rotor sculpting is shown to affect both average torque and torque pulsations. Torque pulsations from a smooth IPM rotor are minimized by utilizing this new analytical model to design sculpt features. The model adequately predicts performance. It not only minimizes specific harmonics of torque but also finds the optimal shape of the sculpt feature taking advantage of the computational efficiency of analytical models. Section 2.2 presents an example IPM machine modeled with this framework's permeance functions, winding functions, and current sources. The winding function framework from [18] is presented based upon the IPM machine's flux sources: the first reluctance path, the second reluctance path, and the magnet path as shown in Figure 1. Included are the necessary modifications to armature MMF to calculate the effects of the equipotential nature of the rotors' salient features. The extended winding function method accounts for rotor surface modifications utilizing an additional MMF term. The integration of the analytical model into the optimization process of rotor sculpting shows a significant improvement in computational effort, is shown in Section 2.3 with the objective to minimize specific orders of torque ripple. The analytical model along with optimization is used to make a smooth rotor machine better with the design of sculpt features. Starting from the FE results of the smooth rotor, the torque harmonics are determined and used to set a target for the analytical method to cancel. The analytical method is used to determine the required sculpt geometry to cancel the targeted torque harmonic.

The analytical model is validated through FE in Sections 3.1 and 3.2. This is because it has been well established that FE results accurately predict airgap fields, and torque characteristics, and is also used in the optimization of IPM machines [24–31].Both smooth and sculpted rotor airgap flux densities and torque are presented and compared. Section 3.3 presents the results of three sculpted rotor designs developed with the analytical model. Analytical design accuracy is validated first by comparing analytical performance to finite elements. Secondly, the geometries of the analytical optimum are compared to the FE optimum. Significant computational savings are demonstrated using the analytical model to minimize torque harmonics.

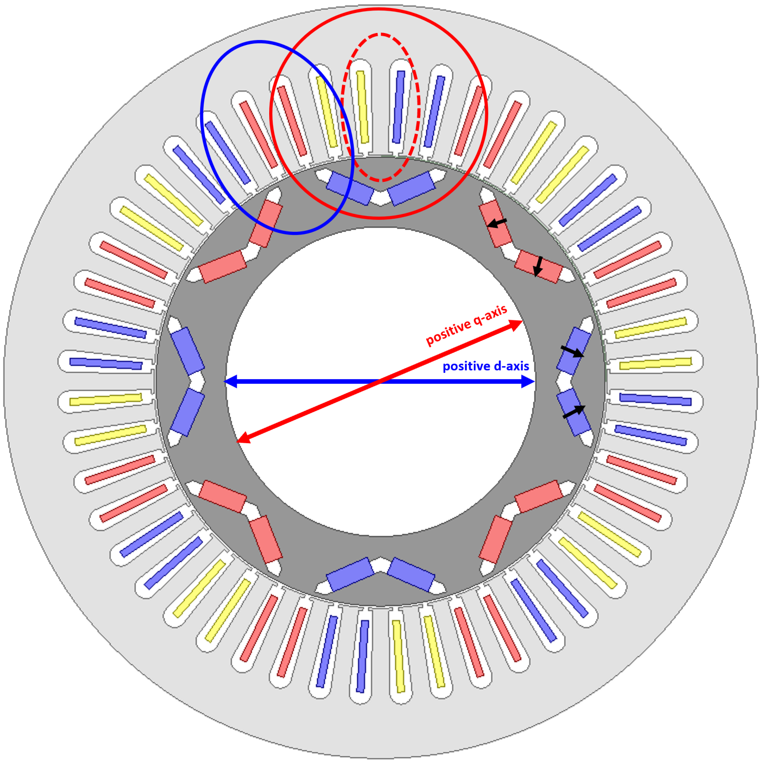

Figure 1. IPM Machine Flux Paths: solid red—first reluctance path, dashed red—second reluctance path, solid blue—permanent magnet, black arrows—magnetization direction.

2. Methods

This section describes the electric machine parameters, sculpt feature geometry, analytical modeling, and optimization method utilized to minimize torque harmonics.

2.1. Electric Machine Parameters

To evaluate the analytical MMF permanence method, a single barrier IPM machine has been modeled using both FE and analytical methods. The model is constructed and evaluated based on a well-known smooth rotor industrial IPM machine. Parameters of this machine are included in Table 1.

A schematic of a two-pole rotor describing the sculpting features of this machine is given in Figure 2. Variables Y_1 and Y_2, define sculpt feature location in terms of half of the magnet pole arc span, α_m, where Y_1 is a positive percentage and Y_2 as a negative percentage (counter-clockwise position). Feature width Z_1 and Z_2, define the sculpt feature width in terms of the percentage of the magnet pole arc span, α_m. A single sculpt feature depth, D_1, is utilized for both features. The asymmetrical features will be used to take advantage of average the possible torque increase but also to target specific torque harmonics.

Table 1. Motor Parameters.

Parameter	Value	Unit
Pole Pairs	4	
Stator Slots	48	
Number of Phases	3	
Stack Length	83	mm
Rotor Diameter	161.15	mm
Airgap Length	0.75	mm
Magnet Pole Arc % of Pole Pitch	63.8	%
Barrier Type	Single V	
Magnet Thickness	6.48	mm
Magnet Width	16 × 2	mm
Permanent Magnet Remnant	1.19	T
Permeability of Iron	∞	$\frac{mkg}{s^2A^2}$
Permeability of Bridge Features	$4\pi \times 10^{-7}$	$\frac{mkg}{s^2A^2}$

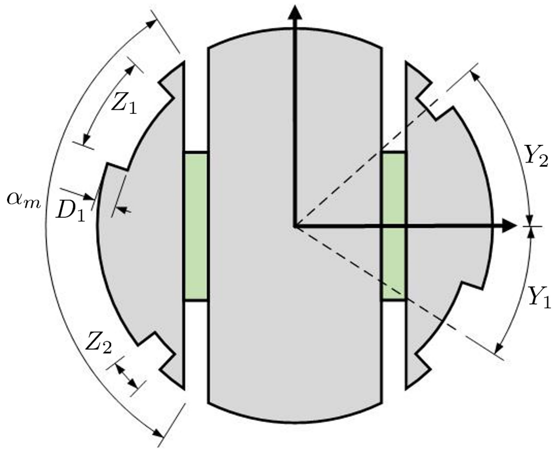

Figure 2. Two pole equivalent sculpted rotor IPM model: gray—iron, green—permanent magnets.

2.2. Analytical Method for IPM Machine Performance Estimation

This section models MMF, F, permeance, Λ, and flux density, B of a slotless armature single barrier IPM machine without saturation. This model, previously developed in [18], forms the basis of the analysis in subsequent sections. An outline of the analytical model solution process is shown in Figure 3 with the subsequent subsections providing further detail.

Conductors are placed at discrete locations, along the circumference of the inner diameter of the stator. Magnets are represented as MMF. Quantities are dependent upon the rotor azimuthian coordinate, θ, and rotor position, ϕ. Winding function theory is employed to construct MMF terms, where the conductor turns function is represented as $n(\phi,\theta)$, the average turns function $< n(\phi,\theta) >$, (2), and winding function is $N(\phi,\theta)$, (1). Separate MMF and permeances are calculated for the machine's first reluctance path, second reluctance path, and magnet path.

$$N(\phi,\theta) = n(\phi,\theta) - < n(\phi,\theta) > \tag{1}$$

$$< n(\phi,\theta) > = \frac{1}{2\pi} \int_0^{2\pi} n(\phi,\theta) d\phi \tag{2}$$

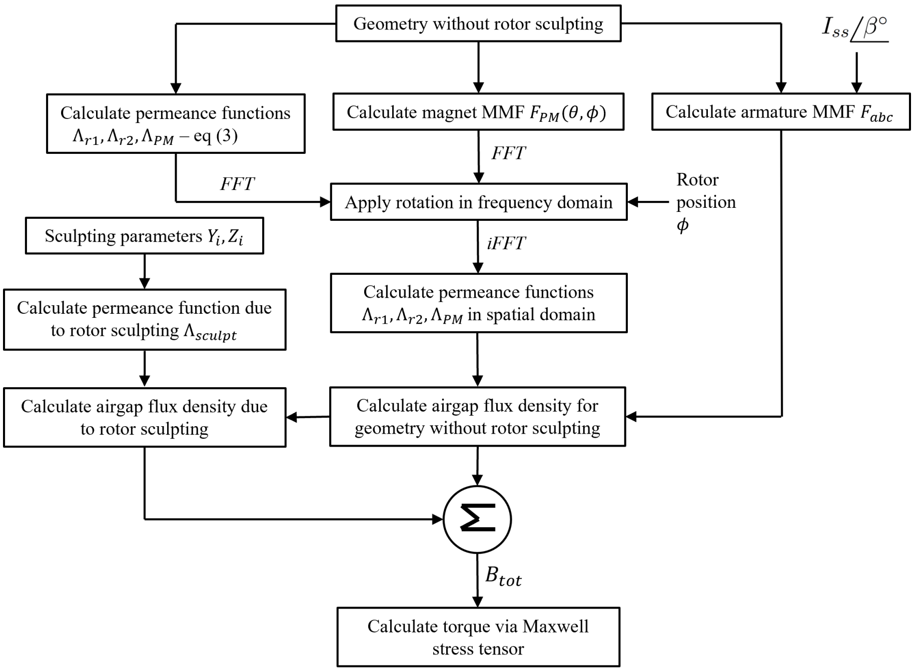

Figure 3. Analytical calculation process for torque accounting for rotor sculpting.

2.2.1. Permeance

Permeance functions result from the geometry of the IPM rotor as shown in Figure 4. Three functions are needed to describe the single-V IPM machine: the primary reluctance path,Λ_{r1}, shown as a solid red line, and the second reluctance path Λ_{r2}, shown as a dashed gray line, and the permeance of the magnet path, Λ_m, shown as a solid gray line. Each function contains a constant and even order harmonics. Permeance functions for the second reluctance path, Λ_{r2}, and magnet path, Λ_{PM}, are based on the winding function, N_{PM}, and related to their respective airgaps, g.

$$\Lambda_{r1}(\phi, \theta) = A_\circ + \sum_{n=2,4,6...}^{\infty} A_n \cos(n\theta - n\phi) \tag{3}$$

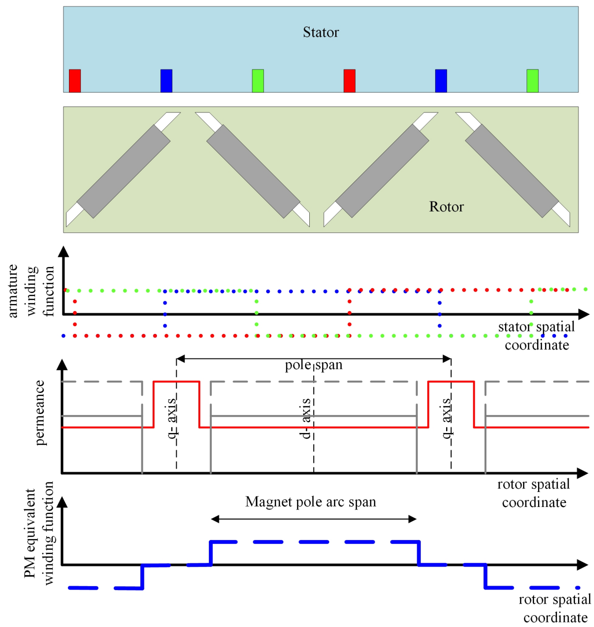

Figure 4. Winding Factor Model of Single V IPM Motor.

2.2.2. MMF

The two fundamentals of MMF sources are shown in Figure 4, the magnet MMF, blue dashed line, and armature, dotted red, green, and blue lines. Additional MMF terms are needed for the second reluctance path, (10), and sculpt features, Figure 5.

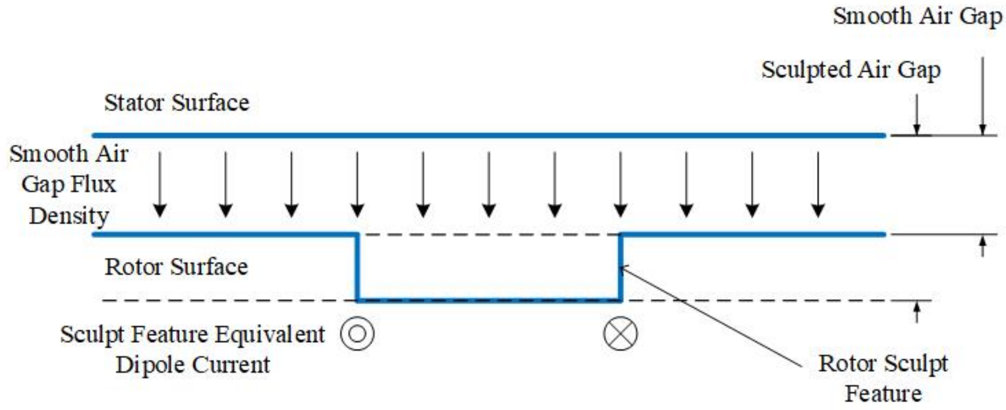

Figure 5. Sculpt Feature Equivalent Dipole Current.

2.2.3. Armature MMF

The phase currents, i_a, i_b, and i_c, are controlled to create a rotating vector and are dependent upon rotor position and the control angle, β. The current alternates for each mechanical rotation proportional to the number of pole pairs p. The armature MMF is the product of the winding function and current for each phase. These winding functions contain only odd harmonics due to the symmetries around the half cycle. Grouping terms, (5) are arranged into positively rotating and negatively rotating sequences. Triplen harmonics do not survive in the armature MMF.

$$F_{abc} = N_a i_a + N_b i_b + N_c i_c \tag{4}$$

$$F_{abc} = I_{ss}\cos(\phi_r)\sum_{v=1,3,5..}^{\infty} a_v \cos v(\theta) + I_{ss}\cos(\phi_r - \frac{2\pi}{3})\sum_{v=1,3,5..}^{\infty} a_v \cos v(\theta - \frac{2\pi}{3}) + I_{ss}\cos(\phi_r - \frac{4\pi}{3})\sum_{v=1,3,5..}^{\infty} a_v \cos v(\theta - \frac{4\pi}{3}) \tag{5}$$

$$F_{abc} = I_{ss}\sum_{v=1,7,13,19..}^{\infty} \frac{3}{2} a_v \cos(\phi_r - v\theta) + I_{ss}\sum_{v=5,11,17..}^{\infty} \frac{3}{2} a_v \cos(\phi_r + v\theta) \tag{6}$$

2.2.4. Magnet MMF

Magnet equivalent MMF is a product of the winding function N_{PM}, equivalent current I_{PM}, and the ratio of magnet pole cap span, τ_m, to magnet total width w_m, as shown in Figure 4. The winding function, N_{PM}, in this case, has been assumed to have one turn. The magnet equivalent current is related to its remnant flux, B_r, the permeability of free space, $\mu_\circ$, relative permeability, μ_r, and magnet thickness, l_m. In this case, the winding function provides the spatial distribution, and the current sets the amplitude of the MMF. Only odd harmonics exist, including the triplen harmonics in the magnet MMF term.

$$F_{PM}(\theta,\phi) = N_{PM}(\theta,\phi) I_{PM} \frac{\tau_m}{w_m} \tag{7}$$

$$N_{PM}(\theta,\phi) = \sum_{v=1,3,5,7,...}^{\infty} b_v \cos(v\theta - v\phi) \tag{8}$$

$$I_{PM} = \frac{B_r}{\mu_0 \mu_r} l_m \quad (9)$$

2.2.5. Second Reluctance Path and Equipotential MMF

Due to the equipotential nature of the rotor second reluctance path, it reacts only to the change of armature MMF across the pole cap, but not the local average. This is illustrated by the second reluctance path airgap flux, shown by the blue dashed line, in Figure 1. Modification to the armature MMF by removing its mean satisfies local conservation of armature flux condition and is made possible through (10). The symbols $F_{<abc>}$ and $< F_{abc}(\theta, \phi) N_{PM}(\theta) >$ represent the modified armature MMF and its average over the span of the second reluctance path.

$$F_{<abc>}(\theta, \phi) = \Big(F_{abc}(\theta, \phi) N_{PM}(\theta, \phi) - < F_{abc}(\theta, \phi) N_{PM}(\theta, \phi) > \Big) N_{PM}(\theta, \phi) \quad (10)$$

$$< F_{abc}(\theta, \phi) N_{PM}(\theta, \phi) >= \frac{\frac{1}{2\pi} \int_0^{2\pi} F_{abc}(\theta, \phi) N_{PM}(\theta, \phi) d\theta}{\frac{1}{2\pi} \int_0^{2\pi} \mid N_{PM}(\theta, \phi) \mid d\theta} \quad (11)$$

2.2.6. Rotor Sculpt Features

Rotor sculpts are designed to modify the radial flux density within the airgap to reduce torque harmonics. This section extends the MMF-permeance method to account for the sculpt features. Winding function theory is extended in [18] to account for rotor sculpt features relying upon EMC currents. Rotor sculpt features modeled with EMC current, I_{ms}, are related to the smooth rotor radial airgap flux density, B_{ms}, sculpt feature depth, l_{ms}, and permeability of free space. The assumption of homogeneous flux density enables breaking the geometry into smaller discrete dipoles (i) of fixed width. The sculpt feature equivalent dipole current is represented by a circle and a cross, as shown in Figure 5. This creates an additional source of MMF across the pole cap of the rotor.

$$I_{ms}(i) = \frac{l_{ms}(i) \cdot B_{ms}(i)}{\mu_\circ} \quad (12)$$

2.2.7. Flux Density

The developed winding function and currents create the MMF sources, F_x, through the machine's permeance paths, Λ_x. Total flux density, B_{tot}, is a combination of four MMF permeance interactions, including: (1) the first reluctance path Λ_{R1} and armature MMF F_{abc}, (2) the second reluctance path Λ_{R1} and modified armature MMF $F_{<abc>}$, (3) the reluctance path of the magnet Λ_{PM} and its MMF F_{PM}, and finally (4) the sculpt feature permeance Λ_{sculpt} and MMF F_{sculpt}. Radial flux density includes odd-order harmonics, including triplen harmonics, due to the interaction between MMF (odd orders) and permeance (even orders). The total radial airgap flux density combines all sources of MMF and permeance. The armature conductors which create the MMF, and, in turn, the radial flux densities also generate localized tangential flux densities. Linear current density is a direct result of the current and conductor locations. Odd order linear current density harmonics are generated but triplen harmonics do not exist when all three phases are combined.

$$B_x(\theta, \phi) = 2\Lambda_x(\theta, \phi) F_x(\theta, \phi) \quad (13)$$

$$B_{tot} = 2\Lambda_{R1} F_{abc} + 2\Lambda_{R2} F_{<abc>} + 2\Lambda_{PM} F_{PM} + 2\Lambda_{sculpt} F_{sculpt} \quad (14)$$

2.2.8. Torque

Torque and its harmonics are calculated from the integration of the Maxwell stress tensor (15). This integration filters out all but harmonic combinations that produce a dc component; combinations of harmonics that do not combine to create an offset do not survive. The result of the integral is multiplied by the square of the airgap radius, r, and the length of the stator stack, l. Each combination of the traveling waves of radial flux density with the tangential linear current density fields gives rise to two possible harmonics, resulting from both addition and subtraction of the harmonic orders. As a result of the rotor position, like orders of radial flux density, B, and linear current density, K, contribute to torque to their nearest multiple of 6, the torque of the machine changes with position.

$$T(\phi) = r^2 l \int_{\theta=0}^{2\pi} B_{tot}(\theta, \phi) K(\theta, \phi) d\theta \tag{15}$$

2.3. Minimization of Torque Harmonics

The developed analytical model is used to design sculpting features upon the smooth rotor machine defined in Table 1. This computationally efficient model is integrated with a genetic optimization tool, GOSET [32], to determine the geometry to minimize the torque ripple via targeted torque harmonics.The integration of the analytical model and optimization algorithm is shown in Figure 6. All optimization is done with a fixed current I_{ss} and angle β, in the constant torque region.

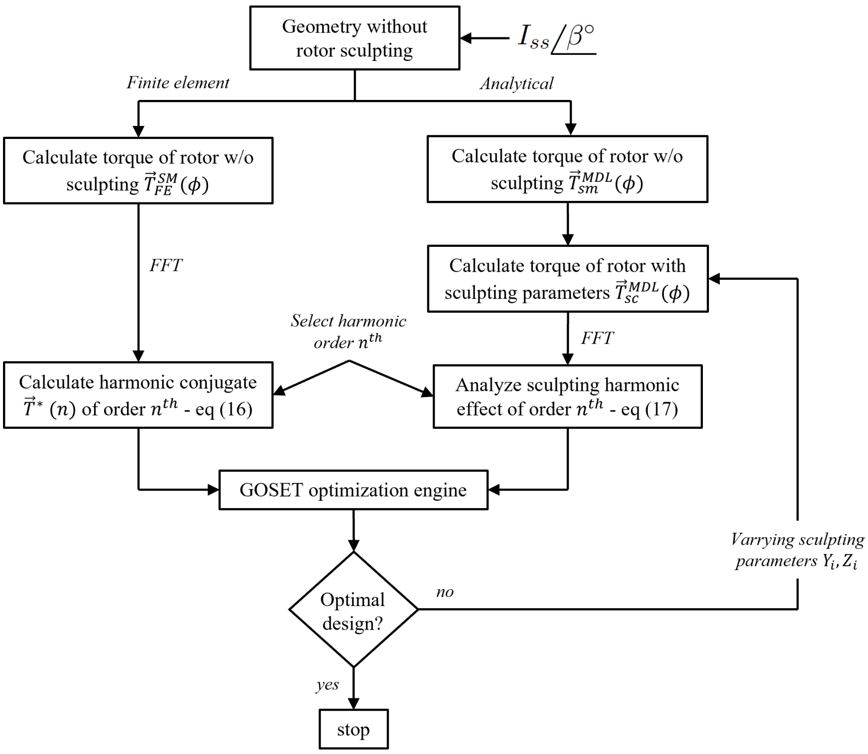

Figure 6. Optimization Process Flow.

Optimization Methodology

The design optimization of sculpt features to minimize the 6th or 12th order torque component amplitude. In previous work, it was shown that the analytical model predicts sculpt feature effects of torque harmonic phase precisely and the amplitude with modest accuracy [18]. Starting with a smooth rotor, optimizing with sculpt features is done using the smooth rotor FE result and the sculpted rotor analytical model. Addressing both the amplitude and phase, the torque harmonic design objective is expressed as a complex number. The targeted smooth rotor FE torque harmonic is rotated 180°, T^*, to determine the desired torque harmonic produced by the sculpt features. Within FE the torque ripple order, torque amplitude, and torque phase are determined. The phase is changed by 180 degrees to use as a command, T^*, allowing the optimization algorithm to design the sculpt features effect upon the smooth rotor. To minimize the torque harmonic, the difference between the finite element smooth rotor torque harmonic conjugate, $\vec{T}^*(n)$ (16), and the analytical models sculpt feature torque harmonic effect, $\vec{T}^{MDL}_{ScEff}$ (17), further defines the optimization objectives in (18) and (19). The torque harmonic conjugate, $\vec{T}^{*}(n)$, is defined by the n^{th} electrical order, and the FE non-sculpted rotor torque harmonic $\vec{T}^{FE}_{sm}$. The analytical models sculpt feature torque harmonic effect, $\vec{T}^{MDL}_{ScEff}$, is defined by the difference of the models sculpted rotor torque, $\vec{T}^{MDL}_{sc}$, and non-sculpted rotor torque, $\vec{T}^{MDL}_{sm}$. Subtracted in complex form, the amplitude of the difference is later used in the objective function. The first, (18) utilizes the sculpt feature location, $Y2$, width, $Z2$, and depth D_1. The second, (19) utilizes the sculpt feature location, Y_1, width, Z_1, and depth D_1. The optimization problems utilize Y_1 are Y_2 to respectively minimize the 6th order and 12th order torque harmonics. Feature locations Y_1 and Y_2 set the phase of the torque harmonics introduced by the sculpt feature [18]. Feature Z_1 and Z_2 are designed to set the amplitude of injected torque harmonic.

$$\vec{T}^{*}(n) = \vec{T}^{FE}_{sm}(n)e^{i\vec{\pi}} \tag{16}$$

$$\vec{T}^{MDL}_{ScEff}(n) = \vec{T}^{MDL}_{sc}(n) - \vec{T}^{MDL}_{sm}(n) \tag{17}$$

$$\begin{aligned} \min_{T,i_d,i_q} \quad & \left|\vec{T}^{*}(12) - \vec{T}^{MDL}_{ScEff}(12)\right| \\ \text{s.t.} \quad & -90\% < Y_2 < 0\% \\ & 2\% < Z_2 < 50\% \\ & |Y_2| + |Z_2| \leq 91\% \end{aligned} \tag{18}$$

$$\begin{aligned} \min_{T,i_d,i_q} \quad & \left|\vec{T}^{*}(6) - \vec{T}^{MDL}_{ScEff}(6)\right| \\ \text{s.t.} \quad & 30\% < Y_1 < 90\% \\ & 2\% < Z_1 < 50\% \\ & |Y_1| + |Z_1| \leq 91\% \end{aligned} \tag{19}$$

The main design constraint of the rotor is mechanical stress. The centrifugal forces coupled with the stress intensification due to the barrier features. Thinner bridges increase magnetic performance but increase stress. For this analysis, the bridge thickness is left constant, and the sculpt feature placement is varied. Stress concentrations occur in either the bridge or sculpt feature as shown in Figure 7. At 5000 rpm the rotor stresses, shown in Figure 8, near yield as the sculpt feature approaches the barrier. A further constraint is applied on feature location in combination with feature size to avoid manufacturing and mechanical limitations of feature placement near the barriers.

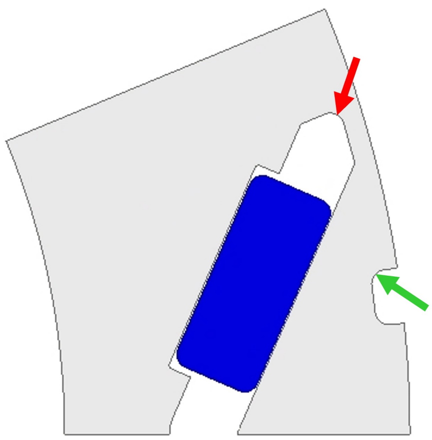

Figure 7. Rotor Sculpt Feature, bridge stress (red arrow), sculpt stress (green arrow).

Each problem was set up with a population of 200 and 10 generations. To confirm the genetic algorithm's accuracy, optimizations were repeated multiple times to confirm stable results.

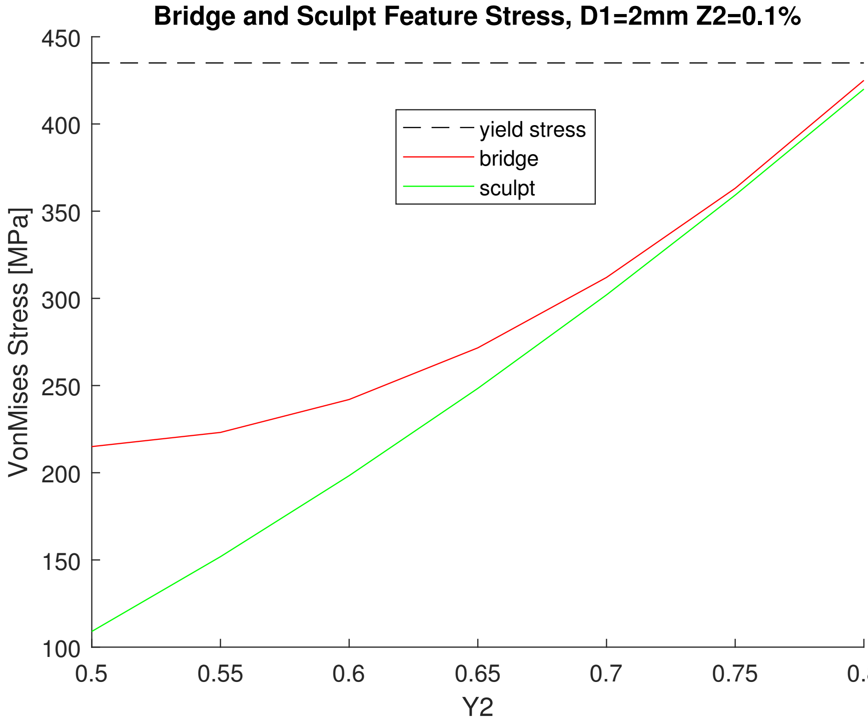

Figure 8. Rotor Stresses, 5000 rpm, D1 = 2 mm, Z1 = 0.1%.

3. Results

The analytical model's permeance structure, stator MMF, and linear current densities are spatially modeled as rectangular pulse trains within MATLAB. The spatial functions are then converted to their Fourier series representation via the Fast Fourier Transform (FFT), enabling efficient rotation models [5]. In place of frequency domain convolution of Fourier coefficients, the spatial domain is reconstructed with the IFFT to determine resulting flux densities. Airgap radial flux densities and linear current density are determined for each position in the spatial domain. Subsequently, the Maxwell stress tensor is employed to determine torque at each position. Once implemented the analytical model solves within 7 s as compared to the finite element model solution taking 15 min. The optimal designs obtained via the analytical approach are achieved at least 72× faster compared to an exhaustive search (full factorial). Further refinement of the design is possible based upon a localized extended search of the analytical design within FE.

3.1. Machine Analysis: Smooth Rotor

The smooth rotor example machine is evaluated for multiple currents I_{ss} and control angles β. Radial flux density and torque are presented in Figures 9–11. The q-axis of the machine is located at a position θ_{elec} of 90° and 270°, the d-axis is at 0° and 180°, where is the θ_{elec} is the rotor azimuthian electrical coordinate. Good agreement with the radial flux density in both Figures 9 and 10. Model and FE torque are compared in Figure 11. Good agreement was observed.

3.2. Machine Analysis: Sculpted Rotor

In Figure 12 a single sculpt feature is added to the rotor. The flux calculated from the analytical model with a sculpt feature is compared to the FE results. Good agreement is seen between FE and the model along with the expected shifting of flux density due to the sculpt feature. Deviations between FE and modeled flux densities are in large part due to fringing that occurs at feature boundaries.

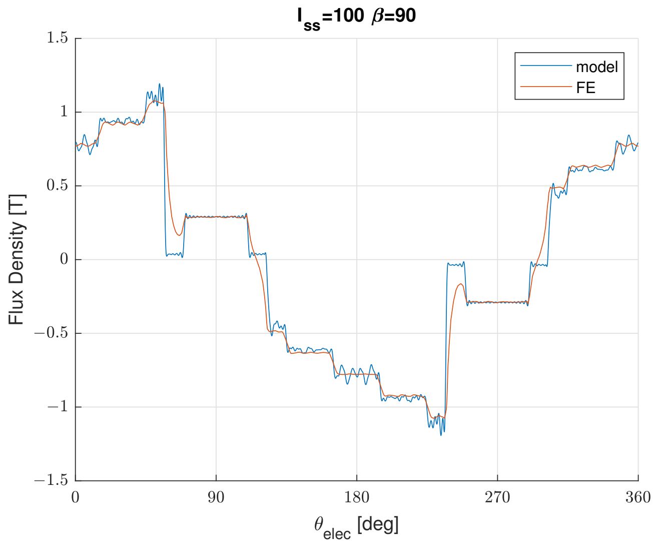

Figure 9. Comparison of Flux Density between FE and Model.

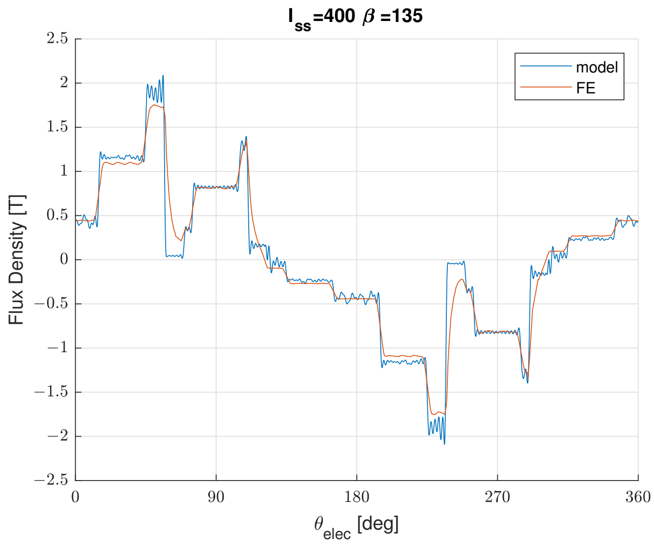

Figure 10. Comparison of Flux Density between FE and Model.

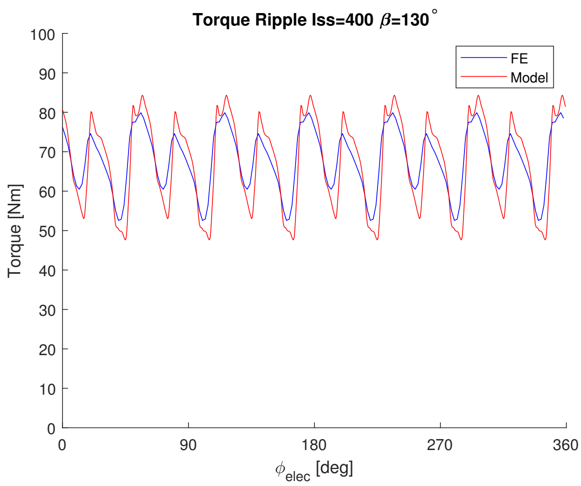

Figure 11. Comparison of Torque Ripple for FE and Analytical Model.

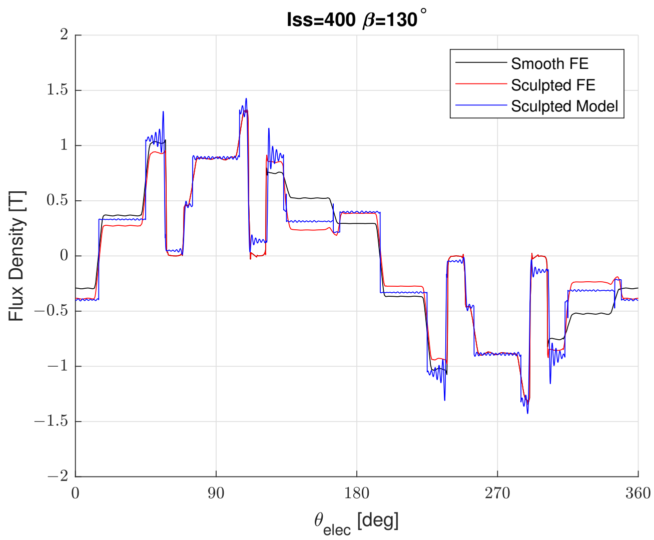

Figure 12. Comparison of Single Sculpt FE and Analytical Model, $Y2 = 50\%$, $Z2 = 20\%$, $D1 = 1.2$ mm.

3.3. Optimal Designs

The optimization process minimized the 12th harmonic or 6th harmonic torque, three designs are of interest. Table 2, highlights these designs. Design 1 designates the starting point of the smooth rotor design. Design 2 and Design 3 seek to minimize the 12th-order harmonic of torque. Design 4 seeks to minimize the 6th order torque harmonic. The optimization of each design using the analytical model required approximately 45 min, whereas an exhaustive search within FE required 72 h. In total, the genetic optimization process results in a 3× speed improvement, and the analytical model results in a 24× speed improvement totaling for a 72× speed improvement.

Table 2. Analytical Model Sculpt Feature Designs.

	Y1	Z1	Y2	Z2	D1
Design 1			smooth rotor		
Design 2	-	-	−86.6%	4.3%	2 mm
Design 3	-	-	−32.1%	20.3%	2 mm
Design 4	75.9%	14.1%	-	-	2 mm

Sculpt feature effects, based on Equation (17), are shown in Table 3 and Figure 13, examining which shows the torque resulting from the analytical design relative to the objective and FE results. Sculpt feature effects on average torque, Table 3, shows reduced average torque for both Design 2 and Design 3. Increased average torque is achieved with Design 4. Chances in both the radial flux density fundamental amplitude and phase account for these changes. Torque amplitude trends are the same for all designs but with limited accuracy. Sculpt feature effects on torque harmonics of the designs are shown in Figure 13. Designs 2 and 3 are shown analytically to achieve the target T^*, when checked in FE Design 2 underachieves the desired torque amplitude, and Design 3 overachieves it. A strong correlation holds between the analytical model sculpt feature torque harmonic effect phase and that found with the finite element model. Design 4 shows a good correlation in the torque harmonic phase between the analytical model and finite element model, and the amplitude shows that the effect on the 6th harmonic is limited.

The three designs proposed to minimize torque ripple, Table 2, are confirmed in FE and shown in Figure 14. Design 2 is shown to reduce average torque 1%, reduce the 6th torque harmonic 3%, and reduce the 12th harmonic of torque ripple by 50%. Design 3 reduces average torque by 8%, increases the 6th harmonic amplitude by 6%, and the 12th harmonic by 75%. Design 4 improves average torque by 1%, reduces the 6th torque harmonic by 17%, and reduces the 12th harmonic by 23%.

Table 3. Comparison of Sculpt Feature Effects to Average Torque (FE and Model), $I_{ss} = 200A$, $\beta = 112°$.

	Model [Nm]	FE [Nm]
Design 2	−0.18	−0.25
Design 3	−1.24	−2.42
Design 4	0.24	0.28

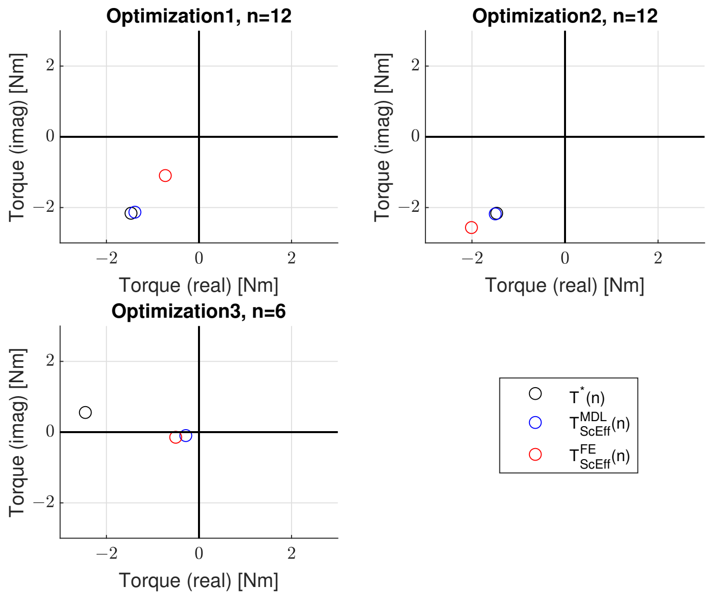

Figure 13. Comparison of Sculpt Feature Design Effects to Torque Ripple (FE and Model) in complex plane for both phase and amplitude, $I_{ss} = 200A, \beta = 112°$.

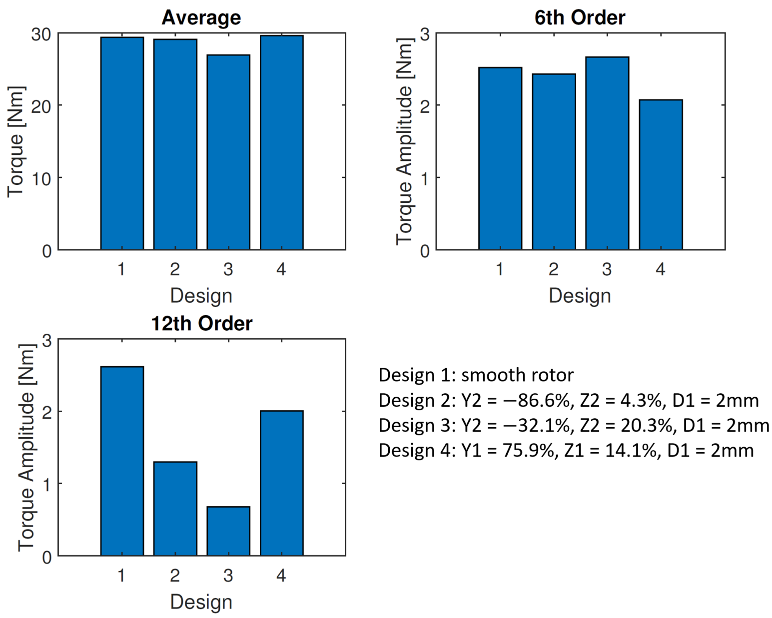

Figure 14. FE Torque Comparison of Analytical Model Optimized Sculpt Features, $I_{ss} = 200A$, $\beta = 180°$.

Finite Element Detailed Search of Design Space

To validate the optimized analytical design, a detailed search, in the region of the designs in Table 2, is performed in FE. Figures 15–17 show the amplitude of the machine's torque harmonic as a function of the design variables. The constraint, $|Y_x| + |Z_x| \leq 91\%$, is represented as a dashed red line in Figures 15 and 17. For all extended searches, the analytical designs are designated with a red asterisk. Comparing Design 2 to extended search results in Figure 15 shows the genes identified in Table 2 are in proximity of the minimum and design optimum within 3%. Full cancellation of the 12th harmonic is not possible with design 2 since the geometry achieving the torque harmonic minimum is beyond the allowable design space. The comparison between design 3 and extended search in Figure 16 shows the analytical design is within the optimum 2% and with a small modification able to fully cancel the torque harmonic. Figure 17, shows that Design 4 cannot fully cancel the intended torque harmonic but is at the minimum along the constraint. For each design, gradients around the optimum are approximately $\frac{0.25Nm}{\%}$ further showing the analytical design sufficiently finds the region of optimum for each design. The new analytical model coupled with GOSET optimization algorithms yields similar geometry and performance as the FE extended search method.

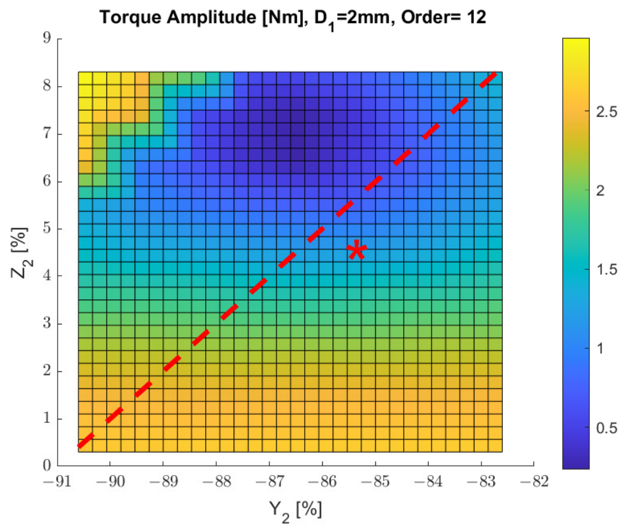

Figure 15. Finite Element Extended Search of Design 2, $I_{ss} = 200A, \beta = 112°$, Constraint: Dashed Red Line, Analytical Design: Red *.

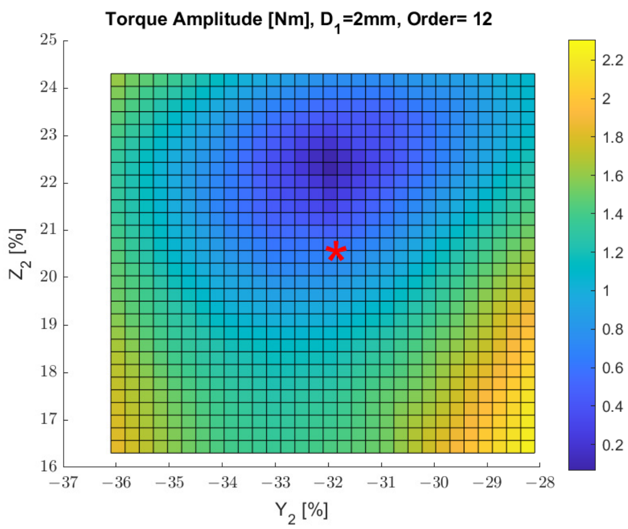

Figure 16. Finite Element Extended Search of Design 3, $I_{ss} = 200A,\ \beta = 112°$, Analytical Design: Red *.

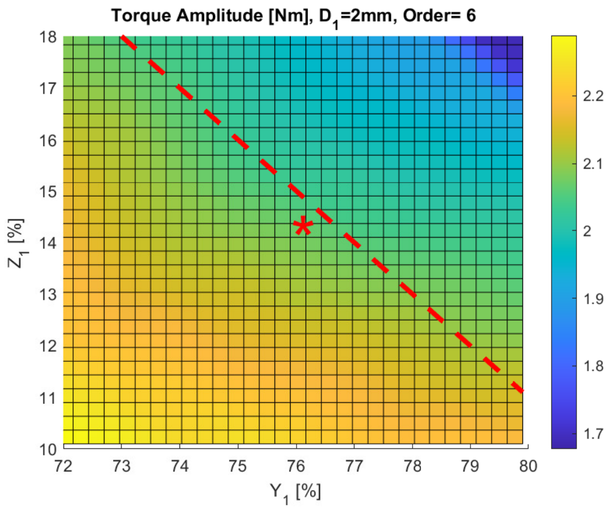

Figure 17. Finite Element Extended Search of Design 4, $I_{ss} = 200A, \beta = 112°$, Constraint: Dashed Red Line, Analytical Design: Red *.

4. Conclusions

This paper has presented an analytical modeling and design optimization approach to reduce torque ripple with rotor sculpt features. By carefully placing rotor sculpt features and rotor barrier features, average torque can be maintained while torque harmonics are minimized. Contributions of this paper include:

1. Asymmetrical sculpting features onto the rotor can address the torque harmonic contents, specifically the 6th and the 12th orders.
2. The analytical model with GOSET optimization yields similar geometry as the benchmarked FE method with an extended search.
3. The analytical model with GOSET optimization yields similar torque pulsation reduction as the benchmarked FE method with an extended search.
4. A single use of the analytical model to design sculpt features has saved significant computational time.
5. Non-standard IPM design can result in a reduction of torque harmonics without a sacrifice of average torque, however, is a cost of additional control complexity.
6. Given a predefined torque harmonic target, an analytical model was developed and used with optimization to design sculpt features to minimize ripple.

Author Contributions: Conceptualization, S.H. and E.S.; methodology, S.H. and T.P.; validation, S.H.; formal analysis, S.H.; investigation, S.H.; writing—original draft preparation, S.H.; writing—review and editing, S.H., T.P. and E.S.; supervision, E.S. All authors have read and agreed to the published version of the manuscript.

Funding: This research received no external funding.

Conflicts of Interest: The authors declare no conflict of interest.

Abbreviations

The following abbreviations are used in this manuscript:

IPM	Interior Permanent Magnet
EMC	Equivalent Magnetic Current
FE	Finite Elements
FFT	Fast Fourier Transform
GOSET	Genetic Optimization System Engineering Tool
IFFT	Inverse Fast Fourier Transform
MEC	Magnetic Equivalent Circuits
MMF	Magnetomotive Force

References

1. Momen, F.; Rahman, K.; Son, Y.; Savagian, P. Electrical propulsion system design of Chevrolet Bolt battery electric vehicle. In Proceedings of the 2016 IEEE Energy Conversion Congress and Exposition (ECCE), Milwaukee, WI, USA, 18–22 September 2016; pp. 1–8.
2. Namiki, K.; Murota, K.; Shoji, M. *High Performance Motor and Inverter System for a Newly Developed Electric Vehicle*; SAE Technical Paper; SAE: Warrendale, PA, USA, 2018.
3. Jurkovic, S.; Rahman, K.; Bae, B.; Patel, N.; Savagian, P. Next generation chevy volt electric machines; design, optimization and control for performance and rare-earth mitigation. In Proceedings of the 2015 IEEE Energy Conversion Congress and Exposition (ECCE), Montreal, QC, Canada, 20–24 September 2015; pp. 5219–5226.
4. Kanayama, T.; Yanagida, E.; Kano, S.; Geller, B.; Nakao, Y.; Fukao, M. *Development of New Hybrid System for Mid-Size SUV*; SAE Technical Paper; SAE: Warrendale, PA, USA, 2020.
5. Hayslett, S.; Van Maanen, K.; Wenzel, W.; Husain, T. The 48-V Mild Hybrid: Benefits, Motivation, and the Future Outlook. *IEEE Electrif. Mag.* **2020**, 8, 11–17. [CrossRef]
6. Han, S.; Jahns, T.M.; Soong, W.L. Torque Ripple Reduction in Interior Permanent Magnet Synchronous Machines Using the Principle of Mutual Harmonics Exclusion. In Proceedings of the 2007 IEEE Industry Applications Annual Meeting, New Orleans, LA, USA, 23–27 September 2007; pp. 558–565.
7. Pellegrino, G.; Guglielmi, P.; Vagati, A.; Villata, F. Core Losses and Torque Ripple in IPM Machines: Dedicated Modeling and Design Tradeoff. *IEEE Trans. Ind. Appl.* **2010**, *46*, 2381–2391. [CrossRef]
8. Yamazaki, K.; Kumagai, M.; Ikemi, T.; Ohki, S. A Novel Rotor Design of Interior Permanent-Magnet Synchronous Motors to Cope with Both Maximum Torque and Iron-Loss Reduction. *IEEE Trans. Ind. Appl.* **2013**, *49*, 2478–2486. [CrossRef]
9. Du, Z.S.; Lipo, T.A. Torque Ripple Minimization in Interior Permanent Magnet Machines Using Axial Pole Shaping. In Proceedings of the 2018 IEEE Energy Conversion Congress and Exposition (ECCE), Portland, OR, USA, 23–27 September 2018; pp. 6922–6929.
10. Liang, J.; Parsapour, A.; Yang, Z.; Caicedo-Narvaez, C.; Moallem, M.; Fahimi, B. Optimization of Air-Gap Profile in Interior Permanent-Magnet Synchronous Motors for Torque Ripple Mitigation. *IEEE Trans. Transp. Electrif.* **2019**, *5*, 118–125. [CrossRef]
11. Yamazaki, K.; Utsunomiya, K. Mechanism of Torque Ripple Generation by Time and Space Harmonic Magnetic Fields in Interior Permanent Magnet Synchronous Motors. In Proceedings of the 2020 International Conference on Electrical Machines (ICEM), Gothenburg, Sweden, 23–26 August 2020; Volume 1, pp. 232–238.
12. Tariq, A.R.; Nino-Baron, C.E.; Strangas, E.G. Iron and Magnet Losses and Torque Calculation of Interior Permanent Magnet Synchronous Machines Using Magnetic Equivalent Circuit. *IEEE Trans. Magn.* **2010**, *46*, 4073–4080. [CrossRef]
13. Koo, B.; Nam, K. Analytical Torque Ripple Prediction Using Air-Gap Permeance and MMF Functions in PM Synchronous Motors. In Proceedings of the 2018 21st International Conference on Electrical Machines and Systems (ICEMS), Jeju, Korea, 7 October 2018; pp. 302–307.
14. Dajaku, G. Open-Circuit Air-Gap Field Calculation of a New PM Machine Having a Combined SPM and Spoke-Type Magnets. *IEEE Trans. Magn.* **2020**, *56*, 1–9. [CrossRef]
15. Li, Q.; Fan, T.; Wen, X. Armature-Reaction Magnetic Field Analysis for Interior Permanent Magnet Motor Based on Winding Function Theory. *IEEE Trans. Magn.* **2013**, *49*, 1193–1201. [CrossRef]
16. Taghipour Boroujeni, S.; Zamani, V. A Novel Analytical Model for No-Load, Slotted, Surface-Mounted PM Machines: Air Gap Flux Density and Cogging Torque. *IEEE Trans. Magn.* **2015**, *51*, 1–8. [CrossRef]
17. Cheng, D.K. *Field and Wave Electromagnetics*; Addison-Wesley: Boston, MA, USA, 1989.
18. Hayslett, S.; Strangas, E. Analytical Design of Sculpted Rotor Interior Permanent Magnet Machines. *Energies* **2021**, *14*, 5109. [CrossRef]
19. Chalmers, B.J.; Akmese, R.; Musaba, L. Design and field-weakening performance of permanent-magnet/reluctance motor with two-part rotor. *IEEE Proc. Electr. Power Appl.* **1998**, *145*, 133–139. [CrossRef]
20. Winzer, P.; Doppelbauer, M. Comparison of synchronous machine designs with displaced reluctance axis considering losses and iron saturation. In Proceedings of the 2015 IEEE International Electric Machines & Drives Conference (IEMDC), Coeur d'Alene, ID, USA, 10–13 May 2015; pp. 1801–1807.
21. Winzer, P.; Doppelbauer, M. A hybrid permanent magnet and wound field synchronous machine with displaced reluctance axis capable of symmetric four quadrant operation. In Proceedings of the 2016 18th European Conference on Power Electronics and Applications (EPE'16 ECCE Europe), Karlsruhe, Germany, 5–9 September 2016; pp. 1–11.
22. Ibrahim, M.; Pillay, P. Aligning the Reluctance and Magnet Torque in Permanent Magnet Synchronous Motors for Improved Performance. In Proceedings of the 2018 Energy Conversion Congress and Exposition (ECCE), Portland, OR, USA, 2–27 September 2018; pp. 2286–2291.
23. Hayslett, S.; Strangas, E. Design and Analysis of Aligned Axis Interior Permanent Magnet Machines Considering Saturation. In Proceedings of the 2019 IEEE International Electric Machines & Drives Conference (IEMDC), San Deigo, CA, USA, 12–15 May 2019; pp. 686–692
24. Merkel, M.; Gangl, P.; Schöps, S. Shape Optimization of Rotating Electric Machines Using Isogeometric Analysis. *IEEE Trans. Energy Convers.* **2021**, *36*, 2683–2690. [CrossRef]
25. Du, Z.S.; Lipo, T.A. Cost-Effective High Torque Density Bi-Magnet Machines Utilizing Rare Earth and Ferrite Permanent Magnets. *IEEE Trans. Energy Convers.* **2020**, *5*, 1577–1584. [CrossRef]

26. Lin, R.; Sudhoff, S.D.; Nascimento, V.C.D. A Multi-Physics Design Method for V-Shape Interior Permanent-Magnet Machines Based on Multi-Objective Optimization. *IEEE Trans. Energy Convers.* **2020**, *35*, 651–661. [CrossRef]
27. Du, Z.S.; Lipo, T.A. Design of an Improved Dual-Stator Ferrite Magnet Vernier Machine to Replace an Industrial Rare-Earth IPM Machine. *IEEE Trans. Energy Convers.* **2019**, *34*, 2062–2069. [CrossRef]
28. Yang, Y.; Bianchi, N.; Zhang, C.; Zhu, X.; Liu, H.; Zhang, S. A Method for Evaluating the Worst-Case Cogging Torque Under Manufacturing Uncertainties. *IEEE Trans. Energy Convers.* **2020**, *35*, 1837–1848. [CrossRef]
29. Jeannerot, M.; Ouisse, M.; Lanfranchi, V.; Dupont, J.-B.; Sadoulet-Reboul, E. Two-level global sensitivity analysis of the excitation contributions leading to acoustic noise in an electric motor for the purpose of robust optimisation. *IET Electr. Power Appl.* **2021**, *15*, 1666–1677. [CrossRef]
30. Sadrossadat, S.A.; Rahmani, O. A framework for statistical design of a brushless DC motor considering efficiency maximisation. *IET Electr. Power Appl.* **2022**, *16*, 407–420. [CrossRef]
31. Ullah, B.; Khan, F.; Milyani, A.H.; Ahmad, N.; Cheema, K.M. Design and analysis of dual-stator hybrid excited linear flux switching machine for long-stroke applications. *IET Electr. Power Appl.* **2021**, *15*, 1678–1691. [CrossRef]
32. Sudhoff, S.D. *Power Magnetic Devices: A Multi-Objective Design Approach*; John Wiley & Sons: Hoboken, NJ, USA, 2021.